communications materials

A Nature Portfolio journal

Article

https://doi.org/10.1038/s43246-025-00934-9

GeSn quantum wells as a platform for spin-resolved hole transport

Prateek Kaul[1,2], Jan Karthein[1,2], Jonas Buchhorn[1,2], Taizo Kawano[3], Taisei Usubuchi[3], Jun Ishihara[3], Nicolas Rotaru[4], Patrick Del Vecchio[4], Omar Concepcion[1], Zoran Ikonic[5], Detlev Grützmacher[1,2], Qing-Tai Zhao[1], Oussama Moutanabbir[4], Makoto Kohda[3] ✉, Thomas Schäpers[1,2,3] & Dan Buca[1] ✉

The nascent group IV GeSn alloys are highly attractive for spintronics applications, including quantum computing, due to their ability to enable highly scalable fabrication and all-electrical spin manipulation. In this work, we conduct an in-depth study of a two-dimensional hole gas in a Ge/GeSn quantum well, exhibiting the integer quantum Hall effect and distinct Shubnikov-de Haas oscillations. Emphasis is given to the determination of the Landé g-factor and its pronounced anisotropy in this two-dimensional system, revealing values significantly higher than those in conventional Ge or SiGe/Ge systems. Moreover, by modeling the spin-orbit interaction using the Iordanskii-Lyanda-Geller-Pikus theory, crucial cubic Rashba spin-orbit interaction coefficients, are extracted and their significance is highlighted. This work provides the experimental validation of the theoretically predicted enhancements in spin-orbit interaction and g-factors in GeSn alloys compared to Ge. Additionally, it delivers essential parameters for the design of hole spin devices, such as hole qubits, utilizing GeSn-based structures on the Si platform.

Spin-based computation, including spintronics[1–3] and quantum processing[4,5] represents a transformative approach to information processing by leveraging the intrinsic spin degree of freedom of electrons alongside their charge. Spin devices such as spin field effect transistors (FETs)[3,6,7] and spin qubits[4,5] hold strong potential for advancing both quantum technologies and low-power consumption electronics, offering advantages in energy efficiency, speed, and scalability. Although spintronics and spin-based quantum processing require different device architectures, the semiconductor components of these advanced devices rely on equivalent material properties. The latter includes low effective masses[8,9], low nuclear spin bath to prevent limitations on spin-coherence[4], high g-factors for higher spin-splitting as well as strong spin-orbit interaction (SOI) in order to have electrically controlled spin-flipping in spin-FETs and spin-qubits.

Group-IV material systems for spin devices provide a compelling platform due to their low abundance of nuclear spins, which can be further isotopically purified to eliminate nuclear spin, as shown already for Silicon (Si)[10] and Germanium (Ge)[11]. Moreover, they can exploit the already established Si-CMOS infrastructure, which has supported significant breakthroughs on the Si platform[12–14] and made Ge especially promising as it provides the highest hole mobility among group IV semiconductors, strong SOI, and relatively large g-factors[15]. Ge's compatibility with the Si-CMOS platform has already enabled significant achievements, such as spin-flipping speeds up to 100 MHz compared to Si[16] and the demonstration of a 4-qubit processor[17].

Building on these advancements, germanium-tin (GeSn) alloys – recently developed group IV semiconductors with properties expected to surpass those of pure Ge - are emerging as strong candidates for spin-based applications[18]. A distinction is the transition from an indirect to a direct bandgap that has been investigated thoroughly for its photonic applications[19–21] and FET electronics[22,23] applications. In addition to the low effective mass of the Γ-valley electrons at the minimum energy in the conduction band, the holes' effective mass also decreases, and SOI and g-factor are expected to be larger. Recent works on GeSn phase-coherent transport[24], optical study of spin-dynamics[25], the 2D hole-gas conduction in undoped[26] and modulation-doped[27] GeSn heterostructures are encouraging results. However, in the previous works on 2DHG in GeSn, key aspects such as effective mass, quantum scattering times, g-factors were not addressed.

[1]Peter Grünberg Institute 9 (PGI-9) and JARA-Fundamentals of Future Information Technologies, Forschungszentrum Jülich, Jülich, Germany. [2]RWTH Aachen University, Aachen, Germany. [3]Department of Material Engineering, Tohoku University, Sendai, Japan. [4]Department of Engineering Physics, École Polytechnique de Montréal, Montréal, QC, Canada. [5]Pollard Institute, School of Electronic and Electrical Engineering, University of Leeds, Leeds, UK.
✉e-mail: makoto@material.tohoku.ac.jp; d.m.buca@fz-juelich.de

Addressing these aspects is crucial for optimizing performance metrics, which are pivotal for achieving high qubit fidelity.

This work provides key studies of the two-dimension (2D) hole gas (2DHG) in Ge/$Ge_{0.92}Sn_{0.08}$/Ge quantum well heterostructures, advancing the field by delivering critical insights into fundamental material parameters such as effective mass, g-factors and Rashba SOI strength for developing a CMOS-compatible spintronics platform using this nascent alloy system. The 2DHG is induced through applied gate bias on gated Hall bar field-effect transistors (FETs). Key parameters, including hole mobility, effective mass, quantum scattering times, and the anisotropy of the g-factor, are extracted from angular and temperature-dependent measurements of Shubnikov-de Haas (SdH) oscillations and Hall resistance quantization steps. Moreover, the SOI is characterized by analyzing the weak localization (WL) to weak anti-localization (WAL) transition, fitted using the Iordanski-Lyanda-Pikus (ILP) model. The results robustly highlight the significance of the cubic component of the Rashba SOI. Notably, the spin-splitting energy and the Rashba cubic coefficient are found to exceed previously reported values for Ge and GeSn systems, reinforcing the potential of GeSn QW heterostructures for fabricating high-performance spin devices, including hole spin qubits.

Results and Discussion

Material and Device characterization

To realize a 2D hole conduction channel, a Ge/$Ge_{0.82}Sn_{0.8}$/Ge quantum well heterostructure is epitaxially grown. The samples are grown on 200 mm Ge buffered Si (100) wafers using an industrial reduced pressure - chemical vapor deposition reactor. First, a 500 nm-thick Ge buffer is grown to reduce the large lattice mismatch between Si substrate and the later GeSn layer. The epitaxy of GeSn is performed at 340 °C, using Ge_2H_6 and $SnCl_4$ as precursors and N_2 as carrier gas, followed by isothermal growth of a 15 nm Ge layer. Details can be found elsewhere[28–30]. The high crystalline quality of the layer stack is confirmed by the high-resolution transmission electron micrograph (HR-TEM) in Fig. 1a. The GeSn layer with a Sn concentration of 8 at.% is pseudomorphic on the Ge buffer, which induces an in-plane biaxial compressive strain of −1.05%. This is confirmed by the X-ray diffraction (XRD) reciprocal space map (RSM), in Supplementary Fig. 2a. The compressive strain lifts the degeneracy of valence band of the $Ge_{0.92}Sn_{0.08}$ layer with the heavy-hole (HH) band at the top of the valence band (explained further below). Additionally, this Sn concentration offers a higher crystal quality than higher Sn content alloys.

The 2DHG is formed in the rectangular GeSn QW, as shown in the simulated band structure, including quantization, in Fig. 1b showing the confined HH levels from the $k \cdot p$ Hamiltonian. The band structure is calculated using a strain-resolved 8-band $k \cdot p$ model, described in reference[31]. For bulk GeSn alloys, both the Sn content and the lattice strain strongly influence the electronic band structures, including the position of the Γ-valley as well as the energy difference between Γ-and L-valleys that defines the "directness" of the semiconductor. However, for the case of valence bands only the lattice strain defines the heavy holes (HH), light holes (LH) and split-off (SO) bands energies, and consequently their energy difference. The energy quantization, however, depends on the well and the barrier thicknesses, as well as the applied electric field (top gate voltage), and adds to the splitting of the HH and LH bands. In the case of compressive biaxial strain, the top VB is the HH sub-band with hole pseudo-spin states J = ± 3/2. The wavefunction density of the first five sub-bands of the confined HH states in the quantum well is also shown in Fig. 1b. A Schrieffer-Wolff transformation is employed to define an effective Hamiltonian (see Supplementary Equations 1-6) from which material parameters are extracted, as discussed later.

Gated Hall bar FETs are fabricated using standard Si process technology, which is presented in detail in Supplementary Fig. 1. We use a 100 nm-thick SiO_2 as gate dielectric in order to minimize the leakage currents for the magneto-transport measurements. A scanning electron micrograph (SEM) of the final device structure is shown in Fig. 1c. The overlap of the gate metal with the ohmic Al/Pt contacts at the source and drain regions ensures better control of the complete conduction channel. The I_d-V_g transfer characteristics for the gate Hall bar transistor measured at 5 K are plotted in Supplementary Fig. 2e. The device works as a p-channel FET because of the 2DHG formation (details below) and low Schottky barrier height of the metal (Al) to the valence band of Ge/GeSn[32]. Further material details and device electrical characterization data can be found in Supplementary section SI-2.

Quantum Hall effect analysis

Magneto-transport measurements are performed using a variable temperature insert system with a base temperature of 1.5 K and maximum magnetic fields B of 14 T. The longitudinal V_{xx}, and transversal (Hall), V_{xy}, voltages are measured under AC currents of 100 nA using standard lock-in techniques (described in Fig. 1c). For angular dependence measurements, the sample is rotated inside the cryostat to achieve different magnetic field orientations with respect to the 2DHG. Clean Shubnikov-de Haas (SdH) oscillations are observed at applied gate voltages above $V_g = -20$ V as exemplified in Fig. 2a. The R_{xx} maxima appears in between the quantized plateaus in the Hall resistance R_{xy}, the steps corresponding to the Landau level filling. They are marked with $1/n$ corresponding to the inverse of the conductance quantum $h/e^2 = 25.8$ kΩ. The Hall plateaus fit very well with the theoretical values, and the R_{xx} drops to zero at low Landau filling factors, proving solely 2D hole conduction with no parallel conduction paths[33,34]. Using the standard Hall formulas (Supplementary Equation 9)[35], the hole mobility (μ) and concentration (n_{2D}), dependent on the gate voltage, is calculated from the slope

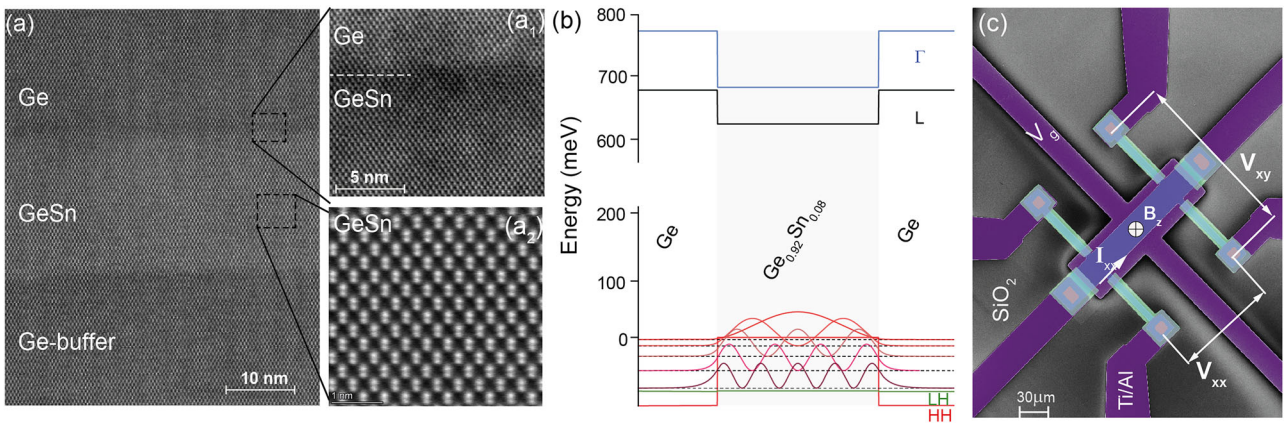

Fig. 1 | GeSn Material and device. a HR-TEM cross-section of the grown Ge/GeSn layer with zoomed images of the marked regions as insets. **b** The electronic band-structure, the first 5 confined HH energy levels and their corresponding wavefunctions **c** Top-view SEM image of the gated Hall bar device annotated with measurement variables.

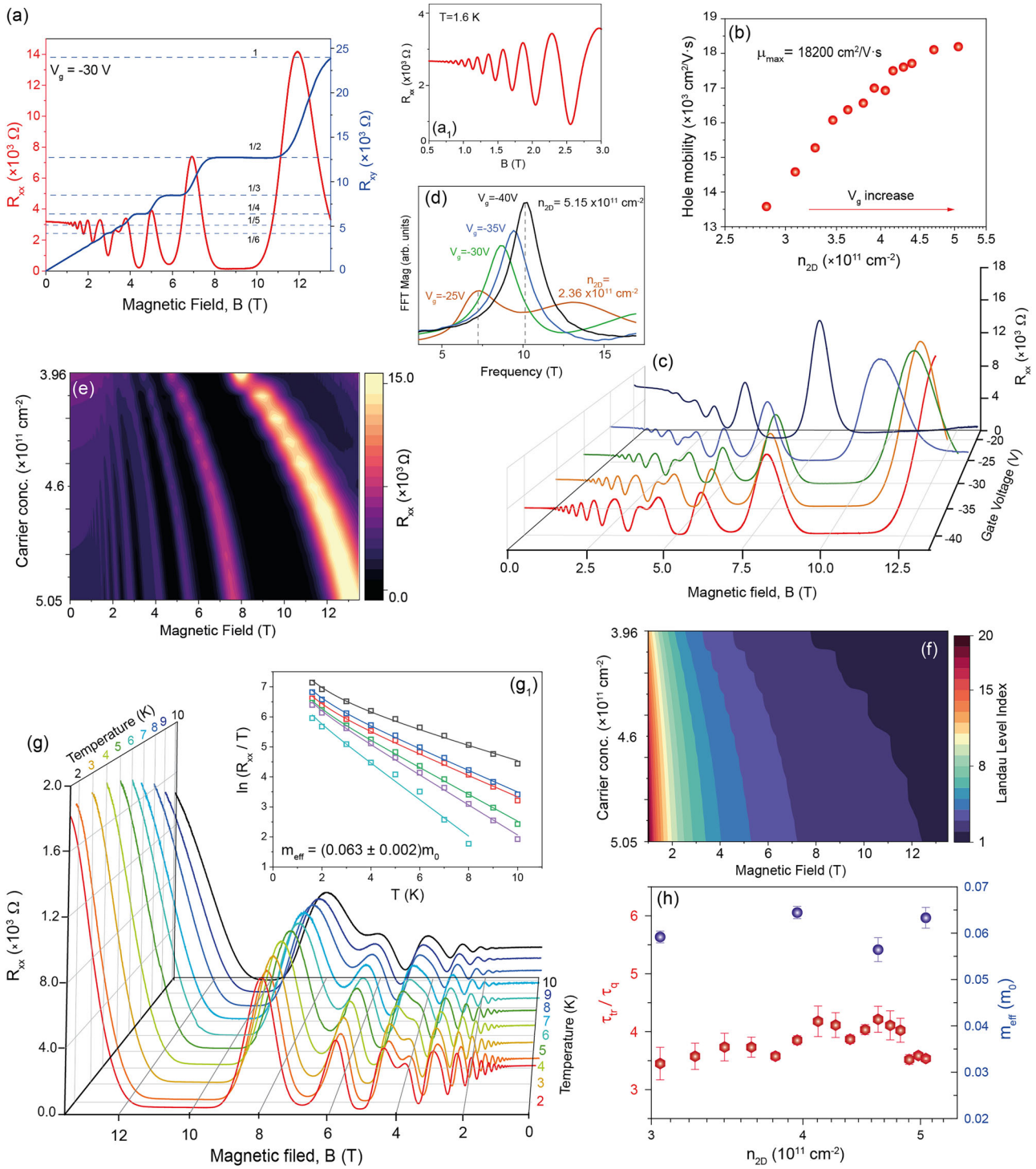

Fig. 2 | Quantum Hall analysis. a R_{xx} and R_{xy} as a function of magnetic field at 1.6 K and $V_g = -30$ V for the gated Hall bar. The dashed lines indicate quantization steps in R_{xy} with 1/n of the conductance quantum (h/e^2). Inset: zoom at low magnetic field. **b** Hole mobility versus carrier concentration extracted using standard Hall equations. **c** 3D plot of R_{xx} at different gate voltages. **d** FFT plots of the SdH oscillations and the extracted 2-D carrier concentration from the frequency peak. Landau fan curve of **f** R_{xx} and **e** Landau filling factor as a function of carrier concentration and magnetic field. The maxima of R_{xx} coincide with the transition lines for LL-levels. **g** Temperature dependent R_{xx} plots from 1.6 K to 10 K The fits for effective mass extraction shown as inset. **h** Ratio of quantum scattering time to the transport scattering time (τ_q/τ_{tr}) and extracted effective mass (in m_0 units) as a function of carrier concentration.

of R_{xy} and R_{xx} at zero field and plotted in Fig. 2b. The carrier concentrations are found to vary from 2.5×10^{11} cm^{-2} to 5×10^{11} cm^{-2} and the mobility increases up to a value of ~18,200 cm^2 V^{-1}s^{-1}. The increase in mobility with the carrier concentration shows screening of scattering mechanisms with increasing carrier density. From the conductivity dependence on the carrier concentration (Supplementary Fig. 3a), a percolation threshold density (n_p) of 1.1×10^{11} cm^{-2} is extracted, which is comparable to undoped SiGe/Ge heterostructures[36], suggesting the viability of future quantum devices on GeSn heterostructures. The R_{xx} signal at different gate voltages is plotted in Fig. 2c and shows an increasing frequency of the oscillations with the gate voltage (Fig. 2d). The values for n_{2D} obtained from the SdH frequency of R_{xx} versus B are in good agreement with the values obtained from the Hall data,

further proof of a single conduction channel. The presence of double peaks for the lowest n_{2D} is an artifact caused by FFT calculation (second harmonic of the main frequency) and not additional conduction channels (FFT analysis in Supplementary Fig. 3b).

The Landau fan diagram for R_{xx} and the Landau filling factor, converted from R_{xy} as 25.8 kΩ/R_{xy} are plotted in Fig. 2e,f. At every value of n_{2D}, the maxima of the resistance appear at the switching of the Landau filling factor and in-between the switching the resistance reaches almost zero (black color). Due to the sufficient high mobility of the holes, the oscillation minima are still visible down to a magnetic field B = 0.5 T, especially for the highest carrier concentration. The depletion of the Landau levels to only the singular level takes place at B = 12 T and already suggests an elevated value of the g-factor. The Landau fan is simulated in Supplementary Fig. 4a; however, it requires further experimental parameters, such as the g-factor, which is discussed in the next section.

The temperature dependence of the SdH oscillations at the highest measured n_{2d} of 5.05×10^{11} cm^{-2} (Fig. 2g), allows for the extraction of holes' effective mass, m_{eff}, in the Ge/GeSn QW as well as the quantum scattering time, τ_q, that sheds light on the scattering mechanisms. The SdH data below B = 4.5 T are used for the m_{eff} determination[24], where the Zeeman splitting contribution can be neglected. Details are provided in Supporting Information file (Supplementary Fig. 3c), and the fits (according to Supplementary Equation 11) are plotted in the inset of Fig. 2g.

The effective mass predicted from the $k \cdot p$ model for the first confined HH sub-band is 0.061 m_0, with m_0 the free electron mass (from Supplementary Equation 7). This value is at the top of the HH band mass, and the non-parabolicity due to the band mixing will lead to a bit larger value of effective mass for higher hole densities in the QW. The extracted effective masses as a function of the carrier concentration shown in Fig. 2h, varies from 0.059 m_0 to 0.063 m_0 due to the high non-parabolicity of the valence band. The values are in good agreement to the effective mass values predicted from the $k \cdot p$ model of 0.061 m_0. Compared to literature data, these values are smaller than for Ge or GeSn values of 0.07–0.1 m_0[37]. This value is reproduced by different devices (see Supplementary Figs. 3d,e) and therefore, can be considered as the in-plane effective mass of the holes in the Ge/$Ge_{0.92}Sn_{0.08}$ system considered here. As the value doesn't change significantly with carrier concentration, for the rest of the analysis presented in this work, an averaged value of 0.061 m_0 is used.

The quantum scattering time (τ_q) is extracted from the fit of the decay of the oscillation amplitude versus $1/B$ using the exponential part of the Dingle equation[24] (Supplementary Equation 12). The transport scattering time, τ_{tr}, which is the average time before an inelastic scattering event occurs, is estimated from the previously calculated mobility and the effective mass as $\tau_{tr} = \frac{\mu m_{eff}}{e}$, where e is the electron charge. The ratio τ_{tr}/τ_q, plotted in Fig. 2h, shows a ratio of ~3–4 for all carrier concentrations (fitting plot in Supplementary Fig. 3f). The relative values of the scattering times close to 1 indicates alloy disorder scattering or interface roughness being the dominant mechanisms for limiting the 2DHG mobility[38,39]. High values, >10, are typically reported in literature for modulation-doped QW structures, where long-range scattering is from the separated layer of dopants responsible for the scattering. Here, the obtained values can be interpreted as a combination of short- and long-range scattering mechanisms. As the GeSn semiconductor is a random alloy, the alloy disorder is expected to contribute to the short-range scattering, whereas scattering at charges/defects at the SiO_2/Ge or Si/Ge interfaces affects the long-range scattering contributions. Therefore, pseudomorphic growth on Ge wafers, and improving the interface quality between the dielectric and top Ge layer are expected to strongly improve mobilities of 2DHG in GeSn even further. An average value below 4 for τ_{tr}/τ_q is a decent value compared to other shallow undoped group-IV QW structures having 1.5[40] and indicates that thicker Ge top layer is beneficial for mobility improvement. The thicker top layer is crucial to screen scattering contributions from the Ge-oxide interface by moving the quantum well deeper, and helps in reducing charge noise and increasing the quantum mobility[41], which enables low noise spin-qubit operation[17,42]. The low effective mass of 0.061 m_0 together with the large mobility, cements the prospects of 2DHG in GeSn structures for applications as HFETs in electronics and as spin-qubits for quantum computing.

Holes g-factor in GeSn QWs

The Landé g-factor describes the responsiveness of the electron or hole spin state to an external field and is a key metric for the strength of spin splitting. The estimation of the g-factor from the quantum Hall effect is performed via angular measurements, where the magnetic field orientation is changed in order to change the Landau level (LL) splitting with respect to the Zeeman splitting. The LL splitting $\left(E_{LL} = \frac{\hbar e B_\perp}{m_{eff}}\right)$ depends only on the perpendicular component of the magnetic field while the Zeeman splitting depends on the absolute magnetic field ($E_z = g\mu_B B$)[43]. The angle-dependent measurements performed at a hole concentration of $n_{2d} = 5.05 \times 10^{11}$ cm^{-2} are plotted in Fig. 3a. As expected, the SdH oscillations vanish for the in-plane orientation of the magnetic field, $B_\parallel$. Replotting the data as a function of the perpendicular magnetic field, $B_\perp$, Fig. 3b, the numbered levels do not adjust in spacing as expected for standard coincidence measurements. This is ascribed to the high anisotropy of the valence band in k-space, which significantly reduces the g-factor when moving from out-of-plane, $B_\perp$, to the in-plane, $B_\parallel$, orientation leading to almost constant SdH oscillation minima positions. Therefore, for holes with anisotropic valence band, like group-IV QW heterostructures based on Ge, alternate methods are usually employed to estimate the g-factor, such as gate-dependent coincidence methods[37,44], temperature dependence of oscillations[45] or angle dependence decay for 2DHG in GaAs[46]. The gate-dependent coincidence relies on tuning the g-factor and, therefore, the Zeeman splitting energy using the gate voltage, as Ge-based systems are shown to have a carrier concentration-dependent g-factor. The carrier concentration dependence is plotted in Fig. 3c, where only the 1, 3, and 5 odd Landau level-indices have a minimum and then only minima at even levels are observed for all carrier concentrations. Therefore, the coincidence is not observed possibly due to the relatively higher carrier concentration compared with the one reported in literature of about 10^{10} cm^{-2} for observing the coincidence. Therefore, temperature dependence of the oscillations similar to reference[45] are used for analyzing the g-factor in the Ge/GeSn QW system.

The temperature dependence of R_{xx} as a function of the Landau-filling factor is plotted in Fig. 3d. From the decays of the minima of different indices, an activation energy Δ_n is extracted using an exponential approximation $\exp(\frac{\Delta_n}{2k_B T})$ and the fits are shown as the inset in Fig. 3d. The odd and even levels depend on different expressions as follows:

$$\begin{aligned} \Delta_{odd} &= g_\perp \mu_B B - \Gamma_B \\ \Delta_{even} &= \frac{heB_\perp}{m_{eff}} - g_\perp \mu_B B - \Gamma_B \end{aligned} \quad (1)$$

where, $g_\perp$ is the g-factor, B the magnetic field, μ_B the Bohr magneton, and Γ_B is used to denote the Landau level broadening as $C\sqrt{B}$ with C as a fitting parameter. The equations are solved for each odd and even pair, (see Supplementary Tables 1,2 for more details) and the averaged g-factor as a function of carrier density is shown in Fig. 3e, alongside literature benchmark of g-factors of Ge 2DHG at similar carrier concentrations[45,47,48]. Similar to compressively strained Ge in SiGe/Ge QW system, the g-factor decreases from ~15 to 13 with the increase in carrier density. However, the addition of Sn enhances this effect by reducing the effective mass and, consequently, increasing the g-factor. The values are large compared to electrons in Si ($g = 2$) or Ge ($g = 2.04$)[49] and also relatively large compared to other 2DEG systems such as InGaAs ($g \sim 5$)[50] and GaSb ($g = 8$)[51] and comparable to InAs ($g = 15$)[52], highlighting the advantages of using GeSn holes for spintronics applications. For calculating the g-factor from the valence band structure in $k \cdot p$ theory, the Luttinger parameter, κ, is required however, it is not known for the GeSn system. A simple linear interpolation between the values of κ for Ge and Sn, yields a relatively small g-factor for the first confined level of 5.5. This indicates that the value of κ deviates significantly and using the presented experimental data, a κ ~ 3.5 is extracted

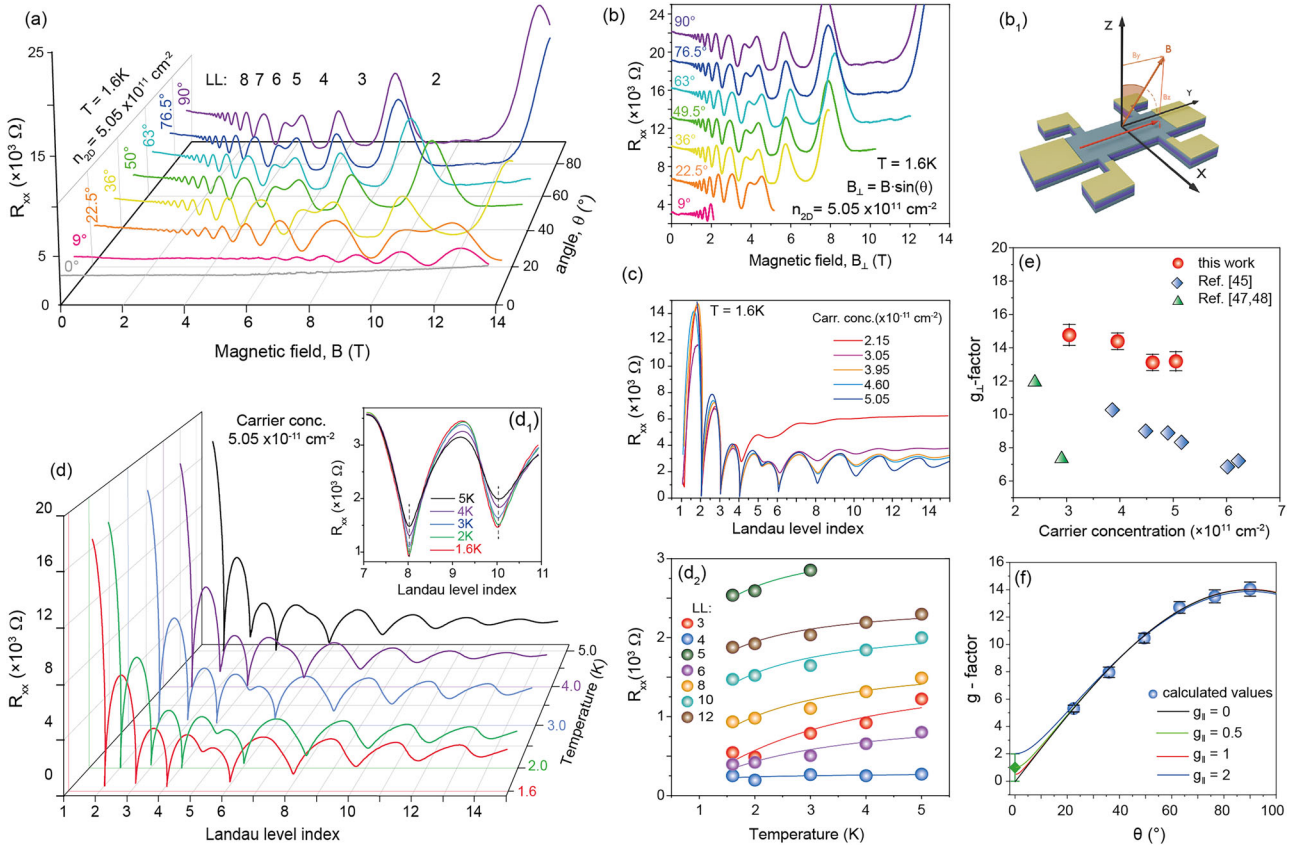

Fig. 3 | Anisotropic g-factor. Angular dependence of R_{xx} on **a** absolute magnetic field, B, and **b** the perpendicular component B·sin θ at 1.6 K and a carrier concentration of 5.05×10^{11} cm^{-2}. The position of different Landau levels (LL) is noted. (b_1) Sketch of experimental measurements. **c** R_{xx} plots as a function of the Landau levels at 1.6 K at different carrier concentrations and **d** at different temperatures for the maximum carrier concentration. The inset (d_1) shows a zoom in the temperature dependence and the (d_2) the fitting plots used for extracting the activation energy $\Delta_{odd\ /\ even}$ for different Landau levels. **e** The out-of-plane g-factor as a function of carrier concentration. Literature data for Ge 2DHG are used as benchmark. **f** Angular dependence of the g-factor showing a strong decrease when moving from out-of-plane to in-plane orientation. Fitting curves plotted alongside for different in-plane g-factor values.

for a $Ge_{0.92}Sn_{0.08}$ quantum well (from Supplementary Equation 7), suggesting high bowing in the alloy. Using this Luttinger parameter κ, the first confined state is found to have a $g_\perp = 13$, being much closer to the experimental value. Furthermore, for completion, the method was also applied at different angular orientations of the magnetic field to obtain the angular dependence of the g-factor, as shown in Fig. 3f. For a heavy hole system, the g-factor is expected to completely vanish under the in-plane direction of the magnetic field[53]. An almost sinusoidal decrease is observed with the g-factor reaching 5 at 20° angle between the B and sample plane, while a value between 0.5–1 by fitting the data with Supplementary Equation 13 for the in-plane g-factor, $g_\parallel$. The latter is predicted from $k \cdot p$ modelling to be around 0.23, which is consistent with the experimental results due to the corrected Luttinger parameter. The Landau fan modelling from newly extracted κ is obtained Supplementary Fig. 4a is obtained, providing similar behavior as observed in the experimental Landau fan, providing robust verification of the g-factor values and Luttinger parameter in the GeSn alloys. This high anisotropy of the g-factor is consistent with the experimental measurements, and the measured high values of g-factor around 15 confirm the 2DHG GeSn system as a strong candidate for implementing spintronics devices in the future.

Characterization of SOI

In order to characterize the spin-splitting caused by the SOI, high-resolution magnetic field scans are performed close to zero magnetic field at different carrier concentrations. The symmetrized magneto-conductance (ΔG) data (Supplementary Fig. 5a for raw data) is shown in Fig. 4a. At low carrier concentrations, a WL effect, i.e., a dip at zero field, is observed, which gradually changes to WAL as the carrier density increases due to the increase in both SOI strength and phase coherence length. To quantify the SOI strength, the conductance plots are fitted using the ILP formalism[54], which allows for estimation of the phase-coherence length (l_φ) and the spin-orbit lengths connected to the linear (l_{SO1}) and the cubic component (l_{SO3}) components of the Rashba SOI, respectively. From the fit (inset of Fig. 4a), a very large value of l_{SO1} (» 100 μm) is obtained indicating almost no spin precession caused by the linear component and that only the cubic component of the SOI is considered responsible. It indicates that the cubic Rashba SOI becomes the dominant contribution. This behavior is also found in Ge QW heterostructures[55,56]. It was also claimed in a previous GeSn 2DHG work, but still only the HLN formalism was used[57] (data for comparison in Supplementary Figs. 5e,f). The definitive proof using the ILP formalism is here demonstrated. The HLN theory considers the Elliot-Yafet spin relaxation mechanism originating from impurity scattering, while the ILP theory assumes D'yakonov-Perel' spin relaxation induced by Rashba SOI. The values extracted using the ILP fits are plotted in Fig. 4b and indicate increasing l_φ to a maximum of (856 ± 5) nm and decreasing l_{SO3} to a minimum value of (242 ± 1) nm, respectively with increasing carrier concentration similar to previous work. Subsequently, the characteristic times are extracted from the fitted lengths using the diffusion constant (D) (according to Supplementary Equation 15) as $\tau_x = l_x^2/D$ and plotted in Fig. 4c. The transport scattering time, τ_{tr} with 0.64 ps at n_{2D} of 5×10^{11} cm^{-2}, is found to be smaller than both τ_φ (17.43 ± 0.19 ps) and τ_{SO} (1.58 ± 0.01 ps) indicating a quantum diffusive regime. Furthermore, the coherence time is inversely proportional to the spin-orbit time, indicating that the D'yakonov-Perel' relaxation mechanism is the appropriate mechanism for spin

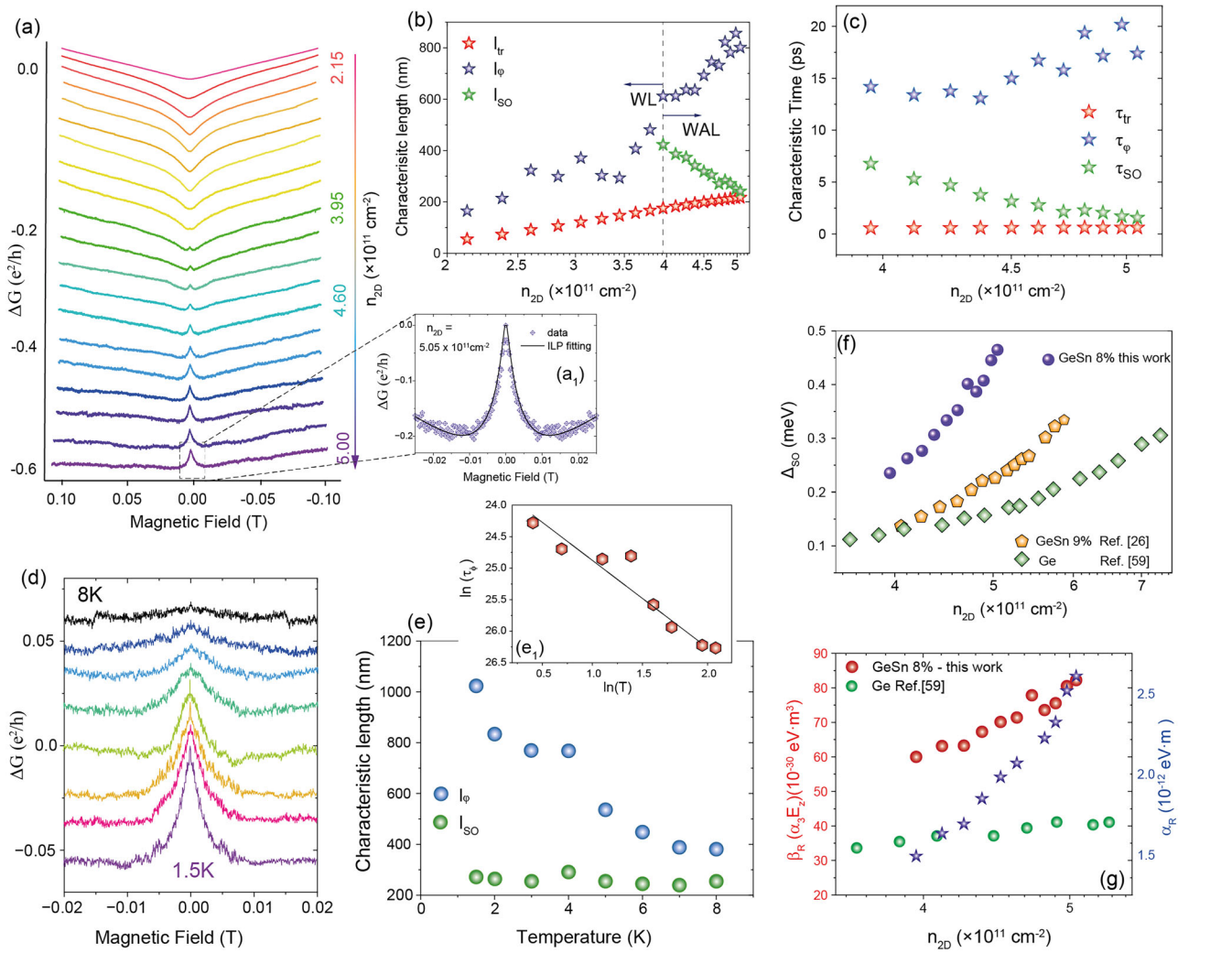

Fig. 4 | Rashba SOI characterization. a Magneto-conductivity (ΔG) in a low field range at different carrier concentrations at 1.6 K (values give on the right). A clear transition from WL to WAL is observed. Data is offset (by 0.03 e^2/h) for better visibility. (a_1) ILP fitting (black) at 5.05 × 10^{11} cm^{-2} shown in the inset. **b** Characteristic lengths (l_{tr}, l_φ, l_{SO}) as a function of carrier density. **c** Characteristic time extracted from the characteristic lengths using the diffusion constants. **d** Magneto-conductivity (ΔG) in a low field range at different temperatures at 5.05 × 10^{11} cm^{-2} density (offset by 0.01 e^2/h). The WAL gradually vanishes with increasing temperature. **e** Temperature dependence of characteristic lengths. (e_1) The inset shows a logarithmic plot of l_φ with temperature with linear fitting (dashed line). **f** Rashba spin-splitting energy dependence on carrier density together with data of previous work on GeSn and Ge QW structures. **g** Cubic Rashba spin-orbit coefficient (red balls, left axis) β_R plotted as a function of carrier density with maximum value of 80 eV-Å^3. Linear Rashba coefficient (blue stars, right axis) α_R calculated for comparison with linear SOI systems.

relaxation. Note that the Elliot-Yafet spin relaxation implies that the coherence time is proportional to the spin-orbit time, which is not the case for our observation. Both of these observations are consistent with the requirements of the ILP fit, and thus definitively prove the presence of cubic Rashba SOI and its increasing contribution with increasing carrier density.

The temperature dependence of SOI is analyzed at the highest carrier concentration (Fig. 4d, other concentrations in Supplementary Fig. 5f). The WAL effect is observed to vanish above a temperature of 7 K. The extracted values of l_φ and l_{SO3} are plotted as a function of temperature in Fig. 4e and only the coherence length is found to decrease with increasing temperature, while l_{SO3} remains constant. The inset of Fig. 4e shows a linear fit with a slope of -1 in logarithmic plot of τ_φ and T, describing the hole-hole interaction being the dominant mechanism for phase-relaxation[58], as is expected for a 2D conduction system.

From the scattering times, the spin precession frequency (Ω_3) is extracted as $1/\tau_{SO} = 2\,\Omega_3^2\tau_{tr}$ and consequently the spin-splitting energy Δ_{SO} is extracted as $\hbar\Omega_3$ to quantify the SOI strength[26]. The values are benchmarked in Fig. 4f together with literature data[26,59]. The plot shows similar behavior with increasing spin-splitting as the hole density increases. In addition, our data shows larger values of (0.462 ± 0.002) meV compared to values in previous reports on similar materials. The cubic Rashba coefficient ($\beta_R = \alpha_3 E_z$, where E_z is the perpendicular electric field) calculated from Δ_{SO} ($\Delta_{SO} = \beta_R k_f^3$, where k_f is the Fermi wave vector in Supplementary Equation 15) is plotted in Fig. 4h and shows almost more than twice increase compared to the Ge reference due to the increased SOI caused by the alloying of Sn. The increase is expected as a simulation of the Rasbha coefficient at zero electric field shows a value of 22 eV·Å^3 for the investigated Ge/GeSn QW compared to only 3 eV·Å^3 for a SiGe/Ge QW system. However, an order increase was not observed experimentally, which hints that further optimizations are required in epitaxy to reach this theoretical prediction. Regardless, the maximum value of 80 eV·Å^3 is close to the highest reported value[60] of 100 eV·Å^3 obtained for an optimized Ge system. For comparison with linear SOI systems the linear term (α_R) is also extracted (although not completely accurate, $\Delta_{SO} = \alpha_R \cdot k_f$) and a maximum value of 2.5 ×10^{-12} eV·m is obtained which is comparable to InGaAs 2DEGs[8,9,60]. The comparison values were obtained in modulation doped QWs and at a much higher carrier concentration, and can also be considered to implement for GeSn in the future. Therefore, affirmative results for SOI strength in GeSn

2DHGs are obtained with very high values of the spin-orbit coefficient, as well as the large tunability of the SOI evident from the switching from WL to WAL in Fig. 4a. Further optimizations in both theory and epitaxy are required to design Ge/GeSn heterostructures to maximize the cubic Rashba SOI in such materials to implement spin-based devices, such as spin-FETs and all-electrical spin-qubits for fast and scalable quantum computing.

Conclusion and outlook

This paper establishes the key parameters underlying hole spin behaviour in GeSn-based 2DHG for spintronic applications, highlighting the potential of the material for spin transport, manipulation, and detection. The holes' transport in heterostructures is characterized by low-temperature magneto-transport measurements. The 2D hole transport is robustly demonstrated via QHE and a hole mobility as high as 18,200 $cm^2V^{-1}s^{-1}$ and a low effective mass of 0.061 m_0, close to the theoretical calculations for in-plane HH effective mass. Scattering time ratio of around 4, highlights relatively low contribution from alloy scattering in limiting the carrier mobility. Angular measurements show strong g-factor anisotropy, expected for a HH system, with a maximum value of 15. The value is higher than for Ge at similar carrier density and is expected to further increase at lower carrier densities. Last but not least, the WL-WAL transition the SOI is evaluated using the ILP model, extracting the cubic component of the Rashba SOI and a large range of τ_{so} is extracted from 6.8 ps to 1.6 ps highlighting significant tuning of the SOI. A maximum spin-splitting energy of 0.46 meV and the a β_R value of 80 eV-Å^3 are found to be higher than previously measured GeSn systems and close to the more mature Ge systems. The results confirm as well as improve over the already established high SOI expected from the alloying of Sn into Ge, as well as provide values of the effective masses and the g-factor consistent with theoretical predictions. Therefore, the work provides ample insight into 2D hole gases in GeSn QWs, and allows further steps in the future for fabricating specialized devices such as gate-defined quantum-dot devices to benchmark the Sn-based alloys for their ultimate potential in spintronics and quantum computing.

Data availability

The datasets generated and/or analyzed during the current study are available from the corresponding authors upon reasonable request.

Received: 30 April 2025; Accepted: 28 August 2025;
Published online: 02 October 2025

References

1. Hirohata, A. et al. Review on spintronics: principles and device applications. *J. Magn. Magn. Mater.* **509**, 166711 (2020).
2. Kohda, M. et al. Perspective on spin-based wave-parallel computing. *Appl Phys. Lett.* **123**, 190502 (2023).
3. Koo, H. C. et al. Control of spin precession in a spin-injected field effect transistor. *Science* **325**, 1515–1518 (2009).
4. Burkard, G., Ladd, T. D., Pan, A., Nichol, J. M. & Petta, J. R. Semiconductor spin qubits. *Rev. Mod. Phys.* **95**, 025003 (2023).
5. Liu, Y., Guan, S., Luo, J. & Li, S. Progress of gate-defined semiconductor spin qubit: host materials and device geometries. *Adv. Funct. Mater.* **34**, 2304725 (2024).
6. Žutić, I., Fabian, J. & Das Sarma, S. Spintronics: fundamentals and applications. *Rev. Mod. Phys.* **76**, 323–410 (2004).
7. Sugahara, S. & Tanaka, M. A spin metal–oxide–semiconductor field-effect transistor using half-metallic-ferromagnet contacts for the source and drain. *Appl Phys. Lett.* **84**, 2307–2309 (2004).
8. Nitta, J., Akazaki, T., Takayanagi, H. & Enoki, T. Gate control of spin-orbit interaction in an inverted $In_{0.53}Ga_{0.47}As/In_{0.52}Al_{0.48}As$ heterostructure. *Phys. Rev. Lett.* **78**, 1335–1338 (1997).
9. Engels, G., Lange, J., Schäpers, T. H. & Lüth, H. Experimental and theoretical approach to spin splitting in modulation-doped $In_xGa_{1-x}As/InP$ quantum wells for B→0. *Phys. Rev. B* **55**, R1958–R1961 (1997).
10. Tyryshkin, A. M. et al. Electron spin coherence exceeding seconds in high-purity silicon. *Nat. Mater.* **11**, 143–147 (2011).
11. Moutanabbir, O. et al. Nuclear spin-depleted, isotopically enriched $^{70}Ge/^{28}Si^{70}Ge$ quantum wells. *Adv. Mater.* **36**, 2305703 (2024).
12. Veldhorst, M. et al. An addressable quantum dot qubit with fault-tolerant control-fidelity. *Nat. Nanotechnol.* **9**, 981–985 (2014).
13. Noiri, A. et al. Fast universal quantum gate above the fault-tolerance threshold in silicon. *Nat.* **601**, 338–342 (2022).
14. Camenzind, L. C. et al. A hole spin qubit in a fin field-effect transistor above 4 kelvin. *Nat. Electron.* **5**, 178–183 (2022).
15. Scappucci, G. et al. The germanium quantum information route. *Nat. Rev. Mater.* **6**, 926–943 (2020).
16. Jirovec, D. et al. A singlet-triplet hole spin qubit in planar Ge. *Nat. Mater.* **20**, 1106–1112 (2021).
17. Hendrickx, N. W. et al. A four-qubit germanium quantum processor. *Nature* **591**, 580–585 (2021).
18. Longo, E. et al. Spin Pumping in Epitaxial Ge $_{1-x}$ Sn $_x$ Alloys. *Adv Quantum Technol* (2024) https://doi.org/10.1002/qute.202400508.
19. Wirths, S. et al. Lasing in direct-bandgap GeSn alloy grown on Si. *Nat. Photonics* **9**, 88–92 (2015).
20. Elbaz, A. et al. Ultra-low-threshold continuous-wave and pulsed lasing in tensile-strained GeSn alloys. *Nat. Photonics* **14**, 375–382 (2020).
21. Seidel, L. et al. Continuous-wave electrically pumped multi-quantum-well laser based on group-IV semiconductors. *Nat. Commun.***15**, 1–8 (2024).
22. Liu, M. et al. Vertical GeSn nanowire MOSFETs for CMOS beyond silicon. *Commun. Eng. 2023* **2**, 1–9 (2023).
23. Junk, Y. et al. Enhancing device performance with high electron mobility GeSn materials. *Adv. Electron. Mater.* 2400561 (2024). https://doi.org/10.1002/AELM.202400561.
24. Kaul, P. et al. Phase-coherent transport in GeSn alloys on Si. *Adv. Electron. Mater* 2400565 (2024) https://doi.org/10.1002/AELM.202400565.
25. De Cesari, S. et al. Spin-coherent dynamics and carrier lifetime in strained $Ge_{1-x}Sn_x$ semiconductors on silicon. *Phys Rev B* **99**, 035202 (2019).
26. Tai, C.-T. et al. Strain effects on rashba spin-orbit coupling of 2D hole gases in GeSn/Ge heterostructures. *Adv. Mater.* **33**, 2007862 (2021).
27. Gul, Y., Myronov, M., Holmes, S. N. & Pepper, M. Activated and metallic conduction in p-type modulation-doped Ge-Sn devices. *Phys. Rev. Appl.* **14**, 054064 (2020).
28. von den Driesch, N. et al. Direct bandgap group IV epitaxy on Si for laser applications. *Chem. Mater.* **27**, 4693–4702 (2015).
29. von den Driesch, N. et al. Advanced GeSn/SiGeSn Group IV Heterostructure Lasers. *Adv. Sci.* **5**, 1700955 (2018).
30. Concepción, O. et al. Isothermal heteroepitaxy of $Ge_{1-x}Sn_x$ structures for electronic and photonic applications. *ACS Appl. Electron. Mater.* **5**, 2268–2275 (2023).
31. Rotaru, N., Del Vecchio, P. & Moutanabbir, O. Hole spin in direct bandgap germanium-tin quantum dot. (2025).
32. Thanailakis, A. & Northrop, D. C. Metal-germanium Schottky barriers. *Solid State Electron* **16**, 1383–1389 (1973).
33. Klitzing, K. V., Dorda, G. & Pepper, M. New method for high-accuracy determination of the fine-structure constant based on quantized hall resistance. *Phys. Rev. Lett.* **45**, 494–497 (1980).
34. von Klitzing, K. et al. 40 years of the quantum Hall effect. *Nat. Rev. Phys.* **2**, 397–401 (2020).
35. Kasap, S. *Principles of Electronic Materials and Devices*. *Hall Effect in Semiconductors* (McGraw-Hill, 1990).
36. Sammak, A. et al. Shallow and undoped germanium quantum wells: a playground for spin and hybrid quantum technology. *Adv Funct Mater* **29**, 1807613 (2019).
37. Lu, T. M. et al. Effective g factor of low-density two-dimensional holes in a Ge quantum well. *Appl Phys. Lett.* **111**, 102108 (2017).

38. Qiu, Z. J. et al. Scattering times in AlGaN/GaN two-dimensional electron gas from magnetotransport measurements. *Solid State Commun.* **131**, 37–40 (2004).
39. Meyer, M. et al. Voltage control of the quantum scattering time in InAs/GaSb/InAs trilayer quantum wells. *N. J. Phys.* **25**, 023035 (2023).
40. Laroche, D. et al. Scattering mechanisms in shallow undoped Si/SiGe quantum wells. *AIP Adv.* **5**, 107106 (2015).
41. Lodari, M. et al. Low percolation density and charge noise with holes in germanium. *Mater. Quantum Technol.* **1**, 011002 (2021).
42. Wang, C. A. et al. Operating semiconductor quantum processors with hopping spins. *Science* **385**, 447–452 (2024).
43. Lei, Z. et al. Electronic g factor and magnetotransport in InSb quantum wells. *Phys Rev Res*. **2**, 033213 (2020).
44. Myronov, M., Waldron, P., Barrios, P., Bogan, A. & Studenikin, S. Electric field-tuneable crossing of hole Zeeman splitting and orbital gaps in compressively strained germanium semiconductor on silicon. *Commun. Mater.* **4**, 1–9 (2023).
45. Drichko, I. L. et al. Effective g factor of 2D holes in strained Ge quantum wells. *J. Appl Phys.* **123**, 32 (2018).
46. Soldatov, I. V., Germanenko, A. V. & Kozlova, N. Extreme g-factor anisotropy of low mobility 2D hole gas in GaAs/$In_{0.2}Ga_{0.8}As$/GaAs quantum well. *Phys. E Low. Dimens Syst. Nanostruct.* **57**, 193–197 (2014).
47. Nenashev, A. V., Dvurechenskii, A. V. & Zinovieva, A. F. Wave functions and g factor of holes in Ge/Si quantum dots. *Phys. Rev. B* **67**, 205301 (2003).
48. Arapov, Y.uG. et al. Contributions of the electron–electron interaction and weak localization to the conductance of p-Ge/$Ge_{1-x}Si_x$ heterostructures. *Low. Temp. Phys.* **33**, 160–164 (2007).
49. Roth, L. M. *g* Factor and donor spin-lattice relaxation for electrons in germanium and silicon. *Phys. Rev.* **118**, 1534–1540 (1960).
50. Lin, Y., Nitta, J., Koga, T. & Akazaki, T. Electron g factor in a gated InGaAs channel with double InAs-inserted wells. *Phys. E Low. Dimens Syst. Nanostruct.* **21**, 656–660 (2004).
51. Dorsch, S. et al. Gate control, g factors, and spin-orbit energy of p-type GaSb nanowire quantum dot devices. *Phys. Rev. B* **103**, L241411 (2021).
52. Irie, H., Akiho, T. & Muraki, K. Determination of g-factor in InAs two-dimensional electron system by capacitance spectroscopy. *Appl. Phys. Express* **12**, 063004 (2019).
53. Mizokuchi, R., Maurand, R., Vigneau, F., Myronov, M. & De Franceschi, S. Ballistic One-Dimensional Holes with Strong g-Factor Anisotropy in Germanium. *Nano Lett.* **18**, 4861–4865 (2018).
54. Iordanskii, Lyanda-Geller, S. V., Yu, B. & Pikus, G. E. Weak localization in quantum wells with spin-orbit interaction. *JETP Lett.* **60**, 199 (1994).
55. Moriya, R. et al. Cubic Rashba spin-orbit interaction of a two-dimensional hole gas in a strained- Ge/SiGe quantum well. *Phys. Rev. Lett.* **113**, 086601 (2014).
56. Failla, M., Myronov, M., Morrison, C., Leadley, D. R. & Lloyd-Hughes, J. Narrow heavy-hole cyclotron resonances split by the cubic Rashba spin-orbit interaction in strained germanium quantum wells. *Phys. Rev. B Condens Matter Mater. Phys.* **92**, 045303 (2015).
57. Hikami, S., Larkin, A. I. & Nagaoka, Y. Spin-orbit interaction and magnetoresistance in the two dimensional random system. *Prog. Theor. Phys.* **63**, 707–710 (1980).
58. Altshuler, B. L., Aronov, A. G. & Khmelnitsky, D. E. Effects of electron-electron collisions with small energy transfers on quantum localisation. *J. Phys. C Solid State Phys.* **15**, 7367–7386 (1982).
59. Chou, C.-T. et al. Weak anti-localization of two-dimensional holes in germanium beyond the diffusive regime. *Nanoscale* **10**, 20559–20564 (2018).
60. Morrison, C. et al. Evidence of strong spin–orbit interaction in strained epitaxial germanium. *Thin Solid Films* **602**, 84–89 (2016).

Acknowledgements

The authors acknowledge financial support from the European Commission for the LASTSTEP Project under grant agreement 101070208, German Research Foundation (DFG) under grant number 537127697, and from the Japan Science and Technology Agency (JST) as part of Adopting Sustainable Partnerships for Innovative Research Ecosystem (ASPIRE), grant number JPMJAP2338.

Author contributions

P.K. and O.C. performed the epitaxial growth and material physical characterization experiments. P.K. fabricated the devices with feedback on fabrication from Q-T.Z. P.K., J.K., and J.B. performed the magneto-transport measurements. T.K. and T.U. J.I. performed the ILP/HLN modeling under the coordination of M.K., T.S., and D.B. planned the experimental work and supervised the experiments. N.R. and P.D.V. performed the theoretical modelling for effective mass calculations (co-verified by Z.I.), g-factors, Landau fans and Rashba SOI terms under the supervision of O.M. T.S., M.K., and D.B. coordinated the data interpretation. P.K., T.S., M.K., and D.B. wrote the manuscript. All authors discussed and agreed on the manuscript.

Competing interests

The authors declare no competing interests.

Additional information

Supplementary information The online version contains supplementary material available at https://doi.org/10.1038/s43246-025-00934-9.

Correspondence and requests for materials should be addressed to Makoto Kohda or Dan Buca.

Peer review information *Communications Materials* thanks the anonymous reviewers for their contribution to the peer review of this work.